An improved technique for characterizing the fracture toughness via scratch test experiments

Ange-Therese Akono [a,*], Franz-Josef Ulm [b]

[a] Department of Civil and Environmental Engineering, University of Illinois at Urbana-Champaign, 3108 Newmark Civil Engineering Laboratory, 205 N. Mathews Avenue, Urbana, IL 61801, United States
[b] Department of Civil and Environmental Engineering, Massachusetts Institute of Technology, United States

ABSTRACT

The scratch test consists in pushing a tool across the surface of a weaker material at a given penetration depth; and it has several applications in Science and Engineering including strength testing of rocks and ceramics, damage of polymers and metals and quality control of thin films and coatings. Despite numerous attempts in the scientific literature, the application of scratch tests to the characterization of fracture properties remains a challenge and a heavily controversial topic. Therefore, this investigation aims at articulating a rigorous theoretical and experimental framework in order to assess the fracture toughness at both the macroscopic and the microscopic length scales, using scratch tests. First, we apply optical microscopy and scanning electron microscopy to investigate the physical evidence of crack initiation, crack propagation and material removal mechanisms during scratch tests. Then, we employ Finite Element simulations of crack growth during macroscopic scratch tests to assess the influence of the blade back-rake angle, the friction coefficient between the blade and the material and the wear flat of the blade on the scratching forces, thus testing the robustness of our Linear Elastic Fracture Mechanics scratch model. Finally, at the microscopic scale, a meticulous scratch probe calibration procedure is described to improve the accuracy of the fracture properties determination by addressing important issues such as moisture content, specimen surface cleanliness and choice of reference material. In summary, we bring forward a robust, convenient and accurate method that is applied to polymers, ceramics and metals and can be further applied to the multi-scale study of fracture processes in complex and challenging materials such as gas shale, cement paste and cortical bone.

Published by Elsevier B.V.

1. Introduction

The scratch test consists in pulling a probe across the surface of a softer material as illustrated in Fig. 1. Although scratch tests are relevant nowadays to several fields of science and engineering, ranging from strength characterization of ceramics [9,24,10] to coating and adhesion of thin films [16–18,21] and wear and damage of metals [2] and polymers [14,15,35], the underlying failure mechanisms are still not fully understood.

Early attempts were made in the late 90s to quantify the scratch deformation mechanisms in polymers as a function of the applied load, and of the scratching probe geometry. For large values of the scratch probe half-apex angle, $\phi > 45°$, Briscoe et al. [14] reported the creation of an elastic reversible groove, for low normal force levels, $F_V < 2$ N, followed by ductile ploughing as the normal load was raised up to 20 N. On the other hand, beyond

20 N and for sharper angles, $\phi < 45°$, micro-cutting processes were observed. The transition from elastic to plastic behavior in scratch testing has been extensively studied by Schirrer and coworkers et al. [15], who developed numerical and analytical solutions to link the residual groove recovery angle to the prescribed strain [30], the initial contact radius, and the friction coefficient between the probe and the material [26]. However, the work of Kurkcu et al. [25] suggests that these models are not valid at a larger scale ($d > 40$ μm or $F_V = 15$ N).

In contrast to ductile deformation mechanisms, little attention has been given to brittle fracture in scratch testing. Wong et al. [35] reported the presence of semi-circular cracks on the residual groove for scratch tests carried out on polypropylene with a spherical probe and with vertical force values greater than 18 N; however, they did not incorporate the fracture properties into their analysis of the scratch response. Williams [34] suggested the existence of a linear relationship between the vertical force and the cube of the groove size, based on the equilibrium crack dimension model developed by Lawn and Fuller [27] for indentation fracture; however, he concluded that micro-cutting in scratch

* Corresponding author. Tel.: +1 217 244 7917.
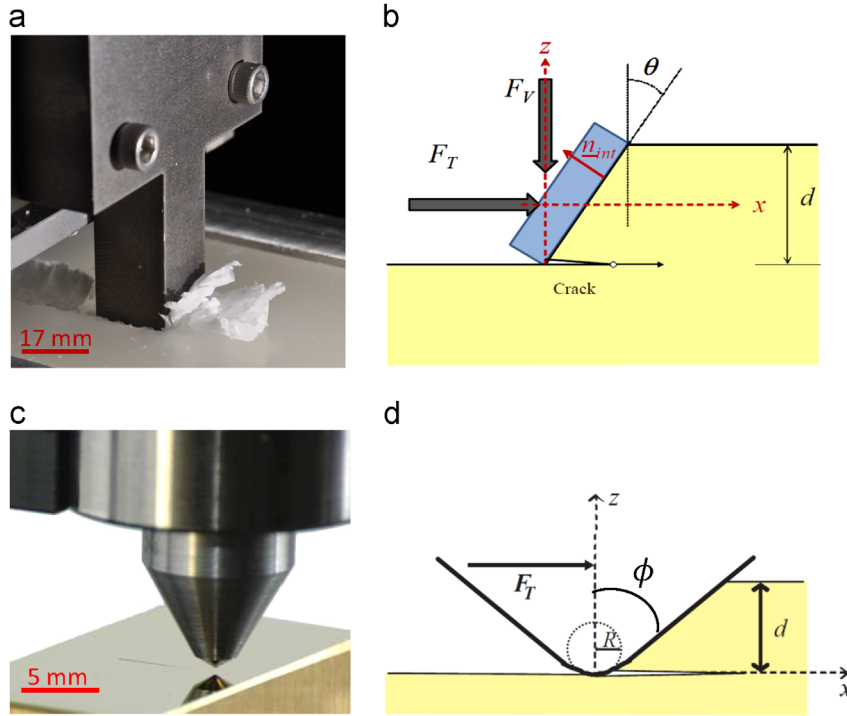E-mail address: aakono@illinois.edu (A.-T. Akono).

Fig. 1. (color online) (a) Macroscopic scratch tests experiments on paraffin wax with a straight parallelepiped steel blade. (b) Idealized 2-D geometry of a macroscopic scratch test: a rectangular blade, making an angle θ with the vertical axis, is pushed horizontally against an elastic material, at a penetration depth d, by applying a vertical force F_V and a horizontal force F_T. (c) 200-μm Rockwell C diamond probe commonly used in microscopic scratch testing applications [9,19]. (d) Idealized representation of a scratch test at the microscopic scale: an axi-symmetric probe, of tip radius R and half-apex angle ϕ, is pulled across the surface of a softer material at a penetration depth d, resulting in a horizontal force F_T.

tests could only be predominant at very large scales (with groove dimensions in tens of millimeters).

The challenge lies in connecting the scratch response to quantifiable material fracture properties while integrating different levels of complexity inherent to the test such as:

- several length scales (the penetration depth, d, can range from nanometers to tenths of centimeter) and force ranges (the vertical force, F_V, can range from millinewtons to thousands of newtons);
- a three-dimensional probe shape (parallelepiped, cylindrical, conical or spherical);
- a variety of deformation patterns (reversible groove, permanent depression or debris generation).

In recent works [4–6], through the application of physical arguments such as Dimensional Analysis [11] and Fracture Energy [22] to scratch testing we demonstrated that the mode of failure (fracture vs. plastic yielding) is influenced by the material properties as well as the geometry of the scratching tool. Moreover, an analytical model based on Linear Elastic Fracture mechanics was constructed to rationalize scratch tests at both the macroscopic (cf. Fig. 1(a)) and microscopic (Fig. 1(c)) length scales. Consider then a horizontal crack emanating from the tip of the scratch probe during a scratch test; the scratch probe being a parallelepiped (cf. Fig. 1 (b)) or axi-symmetric (cf. Fig. 1(d)) and inclined with an angle θ with respect to the vertical axis. Using an Airy stress function $\varphi(x,z)$ under plane conditions, the stress components read

$$\sigma_{xx} = \frac{\partial^2 \varphi}{\partial z^2} = -6bxz + c \tag{1}$$

$$\sigma_{xz} = \frac{\partial^2 \varphi}{\partial x \partial z} = b\left(3z^2 - \frac{3}{4}d^2\right) \tag{2}$$

$$\sigma_{zz} = \frac{\partial^2 \varphi}{\partial x^2} = 0 \tag{3}$$

where the constants (b,c) are chosen so as to satisfy the stress boundary conditions at the material-probe interface (S):

$$\int_{(S)} \underline{\underline{\sigma}} \cdot \underline{n} \, dS = F_T \underline{e}_x - F_V \underline{e}_z \tag{4}$$

Applying the energetic contour-independent J-integral [32] the strain energy release rate, which is the energy required to create a unit fracture surface, reads

$$\mathcal{G} = \frac{1-\nu^2}{E} \frac{F_{eq}^2}{2pA} \tag{5}$$

where $E^* = E/(1-\nu^2)$ is the plane strain elastic modulus; E being Young's modulus and ν being Poisson's ratio. $2pA$ is the *scratch probe shape function* equal to $2(w+2d)wd$ for a parallelepiped blade of out-of-plane width w and to $4(\tan \phi/\cos \phi)d^3$ for a cone of half-apex angle ϕ; d being the penetration depth. Finally, F_{eq} includes the contributions of both the vertical, F_V, and the horizontal, F_T, forces. In particular, the contribution of the vertical force F_T to the fracture process is significant only when the probe is inclined, i.e. $\theta > 0$. In other words, for a parallelepiped tool or a conical probe, the equivalent force F_{eq} reads as follows:

$$F_{eq} = \begin{cases} F_T & \text{if } \theta = 0 \\ \sqrt{F_T^2 + \frac{3}{5}F_V^2} & \text{if } \theta > 0 \end{cases} \tag{6}$$

By entering the expression of the strain energy release rate in the fracture criterion ($\mathcal{G} = \mathcal{G}_f$), which is enforced at the onset of crack propagation, it then becomes possible to link the forces and the

tool geometry to the plane strain fracture toughness $K_c = \sqrt{G_f E^*}$ according to

$$\frac{F_{eq}}{\sqrt{2pA}} = K_c \qquad (7)$$

In this context, the current investigation aims at formulating a theoretical and experimental framework for fracture characterization via scratch tests at both the macroscopic and the microscopic length scales. First, the physical evidence of fracture processes at work during scratch tests is investigated. Second, numerical simulations of crack propagation during scratch tests are performed using the Finite Element software ABAQUS in order to validate the theoretical scratch fracture model described above and investigate the dominant fracture mode. Finally, a painstaking scratch probe calibration procedure is described for microscopic scratch tests, so as to improve the accuracy of the fracture characterization while addressing specific experimental pitfalls such as surface cleanliness, moisture content and choice of reference material.

2. Physical evidence of cracking and chipping processes during scratch tests

In order to elucidate the failure mechanisms at work during scratch testing, a macroscopic scratch tester apparatus was designed and built in-house [3]. Then, paraffin wax specimens were cast from a mix of pure paraffin wax (Polygonwax, MA) and 2% Vybar and prepared for both the compression and the scratch testing. Figs. 1(a), 2(b) and (c) show crack initiation, crack propagation and chip formation mechanisms occurring during the scratch testing of three different specimens of paraffin wax, providing a detailed insight into the sequence of fracture events: as the blade is pushed against the material, a horizontal crack emanating from the tip of the blade propagates ahead, in the scratch direction and then curves upward to create a chip.

This process is repeated again and again, as the blade advances through the material at the prescribed penetration depth.

At the microscopic scale, scratch tests were performed on cold-drawn high-strength carbon steels (a 5-mm tall and 19-mm round cylindrical specimen of steel AISI-1144 and a 5-mm tall and 12-mm round cylindrical specimen of steel AISI-1045, provided by McMaster-Carr, NJ) and ceramic materials (two 12-mm tall and 25-mm round cylindrical specimens of Macor and Silicon Carbide provided by Accuratus, NJ) using a CSM-Instruments Revetest Scratch Tester. Prior to testing, all specimens were first polished according to standard nano-indentation material preparation routines [28], then cleansed with isopropyl alcohol in an ultrasonic bath, and finally oven-dried at 240 °F for 2 h. The specimens were tested with a 200-μm Rockwell C diamond indenter, at a scratching speed of 6 mm/min and with a maximum vertical force equal to 150 N for carbon steels, and 30 N for ceramics. Immediately after scratch testing, both Macor and Silicon Carbide were imaged under an optical microscope, revealing the presence of several micro-cracks and chips as shown in Fig. 2(e) and (f), resulting from the scratch tests.

Regarding the cold-drawn carbon steel specimens, Steel AISI-1144 and Steel AISI-1045, immediately after scratch testing, back-scattered electron microscopy was performed with a Philips XL-30 Environmental Scanning Microscope under high vacuum and with a high accelerating voltage (15–20 keV) in order to image the residual grooves. Fig. 2(c) and (d) shows the presence of residual micro-cracks, regularly spaced, with a direction of propagation parallel to the scratch direction and a crack front curved and perpendicular to the crack direction. Therefore, the experimental observations at both the macroscopic and microscopic length scales suggest the succession of multiple fracture events during a single scratch test. Furthermore, each cracking event is characterized by a three-dimensional fracture surface emanating from the tip of the probe that propagates horizontally—initially—and with a crack front normal to the scratch direction, which is in agreement with the assumptions of our LEFM scratch model. Compared to
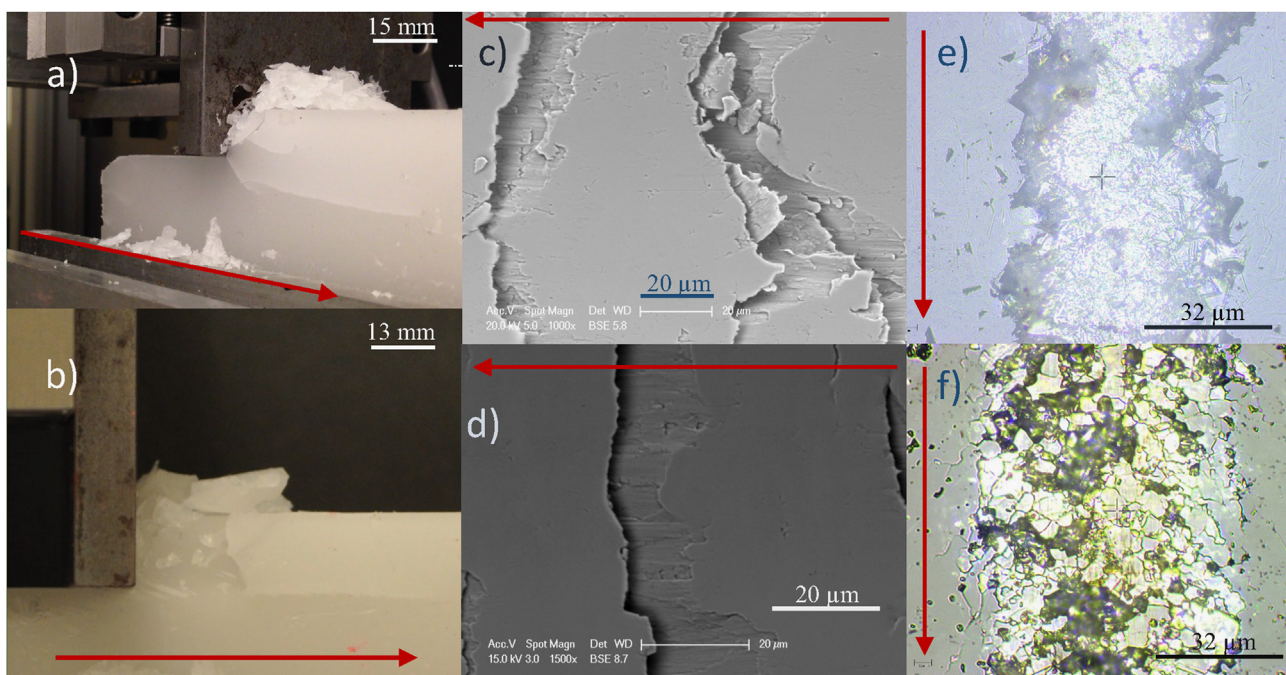

Fig. 2. (color online) Fracture processes in scratch tests at both the macroscopic and microscopic scales: the red arrows indicate the scratch direction. (a) and (b) Crack initiation, crack propagation and chipping mechanisms occurring during the macroscopic scratch testing of two different paraffin wax specimens. (c) (respectively d) Back-scattered electron image of the residual groove of cold-drawn steel AISI-1144 (respectively cold-drawn steel AISI-1045) immediately after scratch testing. (e) (respectively f) Optical image of the residual grove immediately after a microscopic scratch test performed on Macor (respectively silicon carbide).

conventional fracture testing methods such as the compact ten-sion test or the three-point bending test on single-edge notched specimens, the scratch test does not require any initial notch, pre-crack or fatigue crack. Instead, as we have shown in [6], the scratch test intrinsically involves a combination of ductile and brittle failure. Thus, by carefully tailoring the geometry (width-to-depth ratio going to infinity for tests with parallelepiped blades and depth-to-tip radius ratio going to infinity for tests with axi-symmetrical probes), we achieve a fracture-driven state that enables us to probe the fracture resistance. Additionally, the scratch tests makes it possible to sample the fracture properties at different locations in the material, at minimal cost and while using a limited material supply. Having shown the novelty of the fracture assessment method via scratch testing, in the next section we will test the robustness of the analytical model by carrying out numerical simulations of crack growth in ABAQUS.

3. Numerical modeling of quasi-static crack growth during scratch testing

Macroscopic scratch test experiments were simulated with a two-dimensional numerical model developed using the Finite Element software ABAQUS/CAE version 6.13-2. In this investigation, a para-metric study was conducted in order to assess the influence of the blade back-rake angle θ and of the friction coefficient μ between the blade and the material, on the scaling of the measured forces, F_T and F_V. In particular, using the ABAQUS Python development environment, a total of 122 numerical experiments were performed, corresponding to 6 values of the friction coefficient ($\mu = 0.05, 0.1, 0.2, 0.3, 0.4, 0.8$) and to 20 values of the back-rake contact angle ($\theta = 0, 1, \ldots, 20$). The maximum value of $\theta = 20°$ was chosen so as to include the geometrical configuration of commercially available macroscopic scratch testers ($\theta = 15°$) [20], whereas the friction coefficient μ reached high values, 0.8, reminiscent of the sliding friction coefficient for rocks. For each Finite Element Analysis ($0 \leq \theta \leq 20°$, $0.05 \leq \mu \leq 0.8$) a Python script was used to build the numerical model, run the analysis, process the analysis data, extract the history of ($F_T, F_V, \mathcal{G}, K_I, K_{II}$) as functions of the prescribed displacement and write this information to an ASCII file to be later analyzed using MATLAB. In the section below, we detail the geometry as well as the mechanical model and present the results.

3.1. Finite element model

The full scratch test geometry as well as the prescribed boundary conditions is detailed in Fig. 3(a): a rigid blade with a back-rake angle θ pushes against an elastic material at a constant penetration depth $d = 5$ mm in order to advance an initial hor-izontal crack of length 10 mm, the out-of-plane width being $w = 100$ mm. The material Poisson's ratio was set at 0.3 and Young's modulus was set at 133 MPa, which corresponds to the experimental value measured via compression tests performed on cylindrical paraffin wax specimens with a radius of 35 mm and a height of 70 mm [7]. Furthermore, the vertical displacement of the blade, $u_y = 0$, was constrained, whereas its horizontal displace-ment, u_x, was linearly increased from 0 to 0.5 mm. The contact between the blade and the material was frictional characterized by a friction coefficient μ and any interpenetration between the blade and the material was prevented by selecting a penalty contact enforcement ("HARD" CONTACT in the Interaction modulus) in the normal direction. Finally, the option NLgeom was selected to account for geometric non-linearity during the analysis.

3.2. Crack tip mesh

For each couple (θ, μ), the corresponding geometry was meshed using plane strain 8-node quadratic quadrilateral elements (CPE8) as shown in Fig. 3(b). To increase the accuracy of the calculation, the mesh was refined with a total of 5695 elements and 17,444 nodes. The crack was defined, using the Interaction module in ABAQUS, as an edge of length $l_{\mathrm{crack}} = 10$ mm with overlapping duplicate nodes that would separate during the analysis. The crack front was specified with a crack extension direction aligned with the scratch direction. Furthermore, in order to capture the $1/\sqrt{r}$ singularity of the stress field in an elastic cracked material, a ring of second-order Barsoum elements [12] focused on the crack tip was created as illustrated in Fig. 3(c). Each element around the crack tip exhibited an edge collapsed to a zero length, while the mid-side nodes on the remaining adjacent edges were shifted to a quarter position. The stress intensity factors in plane mode would then be accurately evaluated knowing the opening and the shear displacement on the crack lips, close to the crack tip [13]. Finally, a frictional contact with the friction coefficient μ
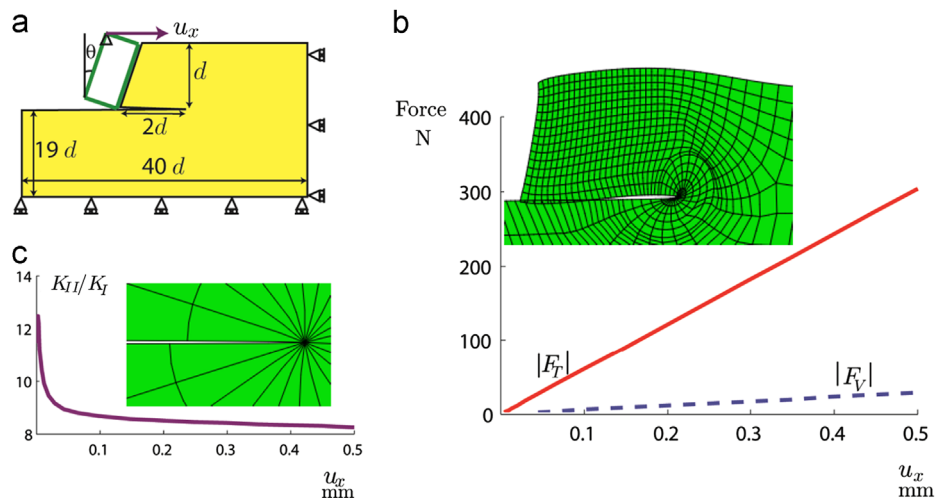

Fig. 3. (color online) (a) Numerical Scratch Fracture model: $0 \leq \theta \leq 20°$ is the blade back-rake angle, $d = 5$ mm is the penetration depth and $0.05 \leq \mu \leq 0.8$ is the coefficient of friction between the blade and the material. During each Finite Element analysis, the horizontal displacement u_x of the blade is linearly increased from 0 to 0.5 mm. (b) Linear force–displacement curves obtained with the parameters ($\theta = 15°$, $\mu = 0.8$); the horizontal force is positive $F_T > 0$ whereas the vertical force is negative $F_V < 0$. For greater accuracy, the mesh was refined as shown here with a magnification scale equal to 15. (c) Evolution of the Stress Intensity Factors in mode I (K_I) and mode II (K_{II}) for ($\theta = 15°$, $\mu = 0.8$). In order to accurately capture the stress singularity in $1/\sqrt{r}$, in the vicinity of the crack tip, the mesh is composed of a ring of second-order quadrilateral elements with collapsed nodes and adjacent mid-side nodes shifted to a quarter location.

was also enforced between the crack lips whereas interpenetration was prevented using the "HARD" CONTACT constraint.

3.3. Energy release rate

Given the prescribed linear elastic behavior, both the vertical, F_V, and horizontal, F_T, forces were linear functions of the pre-scribed displacement u_x as shown in Fig. 3(b). Moreover, in all simulations, the resulting horizontal force was greater in absolute value than the resulting vertical force, which is in agreement with experimental observations on Jurassic limestone, cement paste and red sandstone [6,8]. During the Finite Element analysis, the crack faces separated propping the crack open as shown in Fig. 3 (c). In particular, the stress intensity factor in mode I, normal tensile opening, K_I, is initially zero and then rises to a positive value. This means that the crack first propagates horizontally and then curves upwards to initiate chip formation; this is in agree-ment with the experimental observations on paraffin wax.

The energy release rate, $\mathcal{G}$, energy dissipated per formation of a unit crack surface was calculated using the virtual crack extension method [29] implemented in ABAQUS [1]. In particular, in plane strain, $\mathcal{G}$ is linked to the stress intensity factors in mode I (normal tensile opening) and mode II (plane shearing) via the Griffith–Irwin equation [22]:

$$\mathcal{G} = \frac{1-\nu^2}{E}(K_I^2 + K_{II}^2) \tag{8}$$

Fig. 4 displays the ratio K_{II}/K_I—evaluated at the end of each analysis—as a function of the back-rake angle θ, for all values of the friction coefficient, $0.05 \leq \mu \leq 0.8$. The mode II is highly dominant, especially for large values of θ. In other words, our scratch fracture method enables us to probe the fracture properties under mixed-mode failure, which is a more realistic case. Fig. 3(c) displays the ratio $\mathcal{G}/[F_{eq}/(2pAE^*)]$ of the energy release rate as evaluated by the J-integral to the prediction of the analytical model (cf. Eq. (5)). For all 20 values of the back-rake angle, $0 \leq \theta \leq 20°$ and all 6 values of the friction coefficient, $0.05 \leq \mu \leq 0.8$, the computed energy release rate is extremely close to the theoretical prediction with a relative error less than 8%. Interestingly, even for high friction coefficients, $\mu = 0.8$, between the blade and the material, the friction dissipation remains negligible compared to the fracture dissipation. Moreover, in the case of a parallelepiped blade, the scaling of the applied forces in $\sqrt{d}$ holds even for a large range of values of the friction coefficient and of the back-rake angle: this confirms previous results obtained by applying Dimensional Analysis to experimental scratch tests data on paraffin wax, cement paste, Jurassic limestone and red sandstone [6,8].

3.4. Wear flat of the blade

In Fig. 3(a), the blade shares a single surface with the material. In contrast, we considered the case of a wear flat, where the blade–material interface involves two surfaces, one flat and one inclined, as displayed in Fig. 5. Selecting the highest friction coefficient, $\mu = 0.8$, two simulations were launched, corresponding to the configuration of the in-house macroscopic scratch tester, $\theta = 0$ (cf. Figs. 1(a), 2(a) and (b)); more detail can be found in [3]), and to that of widely used and commercially available macroscopic scratch testers [20]. In particular, the presence of a wear flat does neither change the scaling of the scratch forces in $\sqrt{d}$, nor influence the accuracy of our analytical model. Therefore, our scratch test fracture model is a convenient, highly accurate and robust method to characterize the fracture toughness.
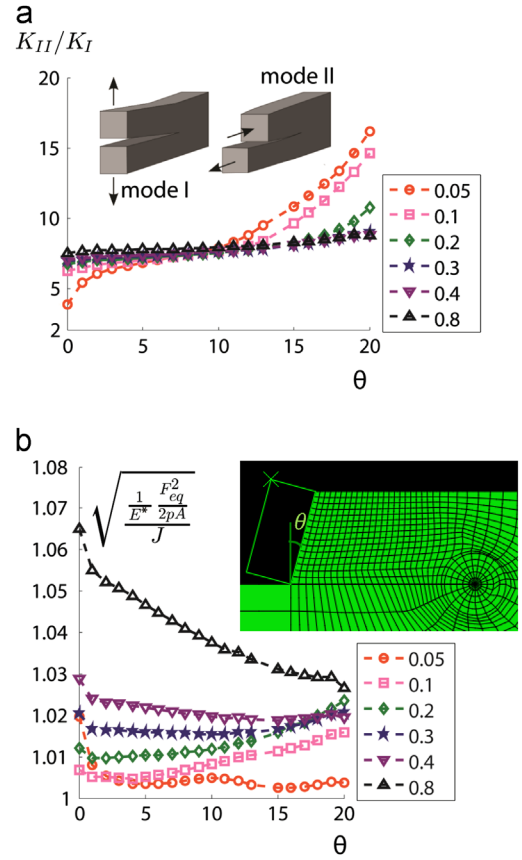
Fig. 4. (color online) (a) Ratio of the stress intensity factor in mode II (in-plane shearing) to the stress intensity factor in mode I (normal tensile opening) as a function of the blade back-rake angle θ. (b) Square root of the ratio of the energy release predicted by the analytical model, $F_{eq}^2/(E^*2pA)$, to the one calculated via the J-integral, J, as a function of θ. E^* is the plane strain modulus, $2pA = 2w^2d$ is the blade shape function and F_{eq} is the equivalent scratch force defined by Eq. (6). Finally, $d = 5$ mm is the penetration depth, whereas $w = 100$ mm is the out-of-plane blade width.
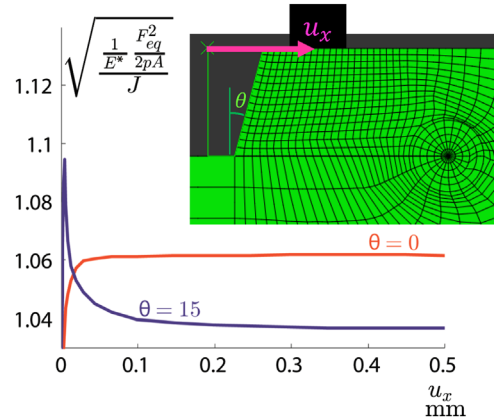

Fig. 5. (color online) Wear flat configuration: the interface between the blade and the material consists of an inclined and a flat surface as shown on the numerical model. Square root of the ratio of the energy release predicted by the analytical model, $F_{eq}^2/(E^*2pA)$, to the one calculated via the J-integral, J, as a function of the prescribed horizontal displacement u_x. E^* is the plane strain modulus, $2pA = 2w^2d$ is the blade shape function and F_{eq} is the equivalent scratch force defined by Eq. (6). Finally, $d = 5$ mm is the penetration depth, whereas $w = 100$ mm is the out-of-plane blade width.

4. Scratch probe calibration procedure

In practice, the method for fracture toughness determination via scratch test, which is based on a robust closed-form theoretical

model and on experimental observations of prevalent fracture processes, also relies on the accurate evaluation of the scratch probe shape function 2 pA. At the macroscopic scale, 2 pA is given by the analytical expression $2wd(w+2d)$, where the blade width w and the penetration depth d can be determined directly. In contrast, at the microscopic scale, the shape function 2 pA needs to be determined indirectly, by calibration with a reference specimen so as to capture any probe defects that could result in significant inaccuracies in the final value of the fracture toughness. To this end, a detailed scratch probe calibration was given in [5]. However, in this section we address specific experimental pitfalls such as the influence of moisture content or surface impurities and the choice of reference material.

The probe of choice is the 200-μm Rockwell C diamond probe, which is commonly used in the quality control of thin films and coatings [9,19]. In particular, the probe geometry consists of a cone of half apex angle $\phi = 60°$ ending in a half-sphere of radius $R = 200$ μm. As illustrated in Fig. 6, the structural integrity of the probe is a great concern, especially when probing hard materials such as ceramics or metals. For instance, optical imaging reveals the presence of cracking on a damaged tip (Fig. 6(a)), which is not present on a flawless probe (Fig. 6(b)). Therefore, the first step to ensure an accurate measure of the fracture toughness at the microscopic scale is to image the probe under an optical microscope to verify that there is no cracking and then clean the probe by gently brushing its tip with a cotton swab saturated in isopropyl alcohol.

4.1. Moisture content

The recommended reference material is Lexan 9034, which is a standard grade of transparent polycarbonate with a known fracture toughness of 2.69 MPa√m [23] and that can be easily purchased from common plastic manufacturers such as SABIC Innovative Plastics, MA. Although polymer samples are typically rigorously flat and therefore do not require polishing, the challenge

consists in removing residual surface impurities as well as moisture content to prevent any local loss of mechanical performance due to degrading processes such as hydrolysis [31]. To this end, a painstaking preparation procedure was designed that involves four steps:

1. Ultrasonic cleaning for 5 min consecutively in a 1% Alconox solution, followed by distilled water.
2. Showering step that consists in exposing all faces to a jet of running distilled water.
3. Oven-drying at 250 °F in clean glass jars and for 24 h to ensure a low moisture content.
4. 24-h cooling period with the specimen laying in a closed glass jar with tight lids and at room temperature.

After rinsing the specimen under running water, any further contact with the surface to test should be avoided. Fig. 7 illustrates the importance of the preparation procedure. A series of 23 scratch tests of length 3 mm and set 2-mm apart were performed on two 25-mm × 25-mm × 12-mm Lexan 9034 specimens at a scratching speed of 6mm/min: the first specimen (BEFORE) was in the initial state as provided by SABIC Innovative Plastics, MA, whereas the second one (AFTER) had been cleansed and dried as described above. The maximum vertical force was 30 N for all tests. Furthermore, prior to testing, each specimen was glued unto a 25-mm square 12-mm thick stainless steel plate and mounted on the CSM-Instruments scratch rectangular holder in order to minimize the displacement compliance during scratch testing. Before cleansing, the top surface exhibits dark stains reminiscent of impurities, dirt and contaminants. In turn, the combination of surface contaminants and high moisture content creates a thin film of material with degraded and inhomogeneous mechanical properties, resulting in measured horizontal forces that are low with a great scatter as shown in Fig. 7(a). On the contrary, after cleansing, the true homogeneous properties of the bulk material are revealed as all 23 scratch test curves in Fig. 7(b) collapse—almost perfectly—on top of each other. Therefore
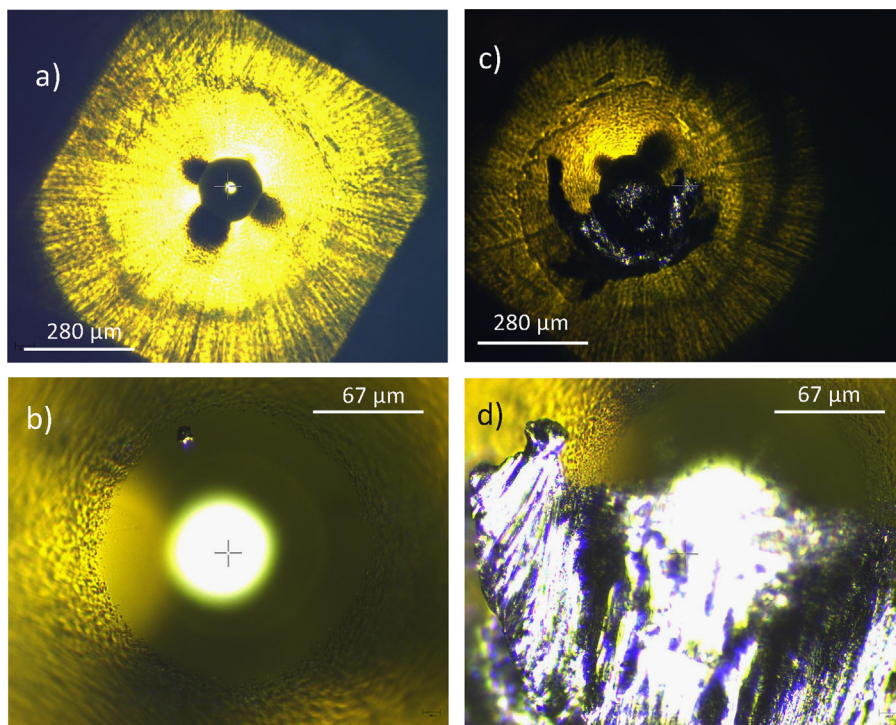

Fig. 6. (color online) Example of damage to the scratch probe as a result of misuse or testing hard materials (such as ceramics). (a) and (b) Optical images of an intact probe at different levels of magnifications, 5 × and 20 × . (c) and (d) Optical images of a broken probe showing intense and irregular cracking at the tip.
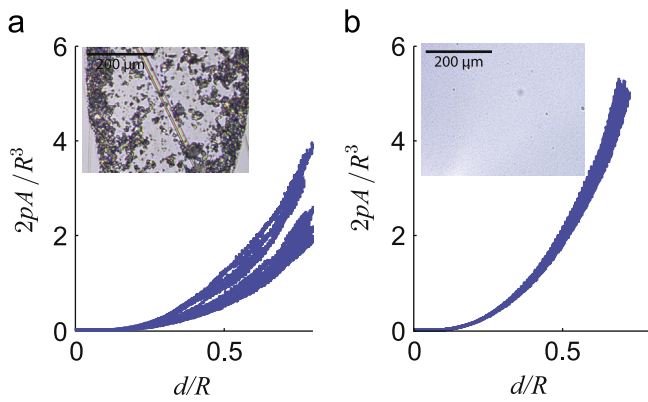
Fig. 7. (color online) (a) Lexan 9034 specimen as provided by Sabic Innovative Plastics. Optical image of the top surface and calibration curve. (b) Lexan 9034 specimen after applying a meticulous preparation procedure that involved consecutively: (1) an ultrasonic bath in a 1% Alconox solution, (2) oven-drying at 240 °F for 48-h and (3) a 24-h drying period in clean tight glass jars at room temperature. Optical image of the top surface and calibration curve. The calibration curve, $2pA(d)$, was calculated by performing 23 3-mm scratch tests with a single 200-μm Rockwell C diamond probe and analyzing the scratch test data using Eq. (7), the fracture toughness of Lexan 9034 being $K_c = 2.69$ MPa$\sqrt{m}$ [23]. (a) and (b) correspond to two 25-mm $\times$ 25-mm $\times$ 12-mm Lexan 9034 specimens, machined from the same 12-mm thick Lexan 9034 sheet, and to the same undamaged 200-μm Rockwell & C diamond probe. 2 pA is the shape function of the probe and d is the penetration depth.

Fig. 8. (color online) Influence of surface contaminants on the calibration curve. In the asymptotic case of a conical probe ($d \gg 26$ μm), the shape function, 2 pA, of a 200-μm Rockwell C diamond probe is given by αd^3, where d is the penetration depth. The same scratch probe, of serial number D-214, was used to test seven 25-mm $\times$ 25-mm $\times$ 12-mm Lexan 9034 specimens that were prepared according to the procedure described in Section 4.1. Optical imaging was subsequently used to discriminate between dirty specimens—with stains and impurities at the surface—and clean specimens—exhibiting a flawless and spotless surface.

ultrasonic cleaning and oven drying are crucial steps in the material preparation procedure.

4.2. Surface cleanliness

Seven Lexan 9034 specimens were prepared following the routine described in Section 4.1. However, new steps were added to induce the accumulation of surface impurities on some specimens. This alteration consisted in storing the specimens in tight closed glass jars at room temperature for 4 days after performing steps 1–3 in Section 4.1. The specimens were then oven-dried a second time for 24 h at 240 °F, to release all moisture content, and finally cooled for 24 h prior to testing. Optical imaging was employed to discriminate between clean specimens with a clear surface, and dirty ones, with a tarnished surface.

All seven Lexan 9034 samples were then tested with a single 200-μm Rockwell C diamond probe, of serial number D-214. Fig. 8 plots the values of the conical calibration coefficient $\alpha = 4(\tan \phi / \cos \phi)$ for both levels of surface cleanliness (clean or dirty). For all three clean specimens, the conical coefficient α varies from 11.87 to 13.47, close to the theoretical estimate, 13.86, for a cone of half-apex angle $\phi = 60°$. In contrast, for three dirty specimens, the value of α is lower, ranging from 9.38 to 9.58. As said before, surface impurities and contaminants generate a thin layer of material with degraded mechanical properties leading to erroneous calibration curves. In this case, we have an outlier, a dirty specimen yet with a high conical calibration coefficient. However, this could be because the depth of the degraded layer is small compared to the maximum depth of penetration. In all cases, the cleanliness of the surface appears to be of paramount importance to obtain an accurate and precise calibration of the scratch probe shape function.

4.3. Reference material

To assess the sensitivity of the fracture toughness determination method with respect to the reference material, two different reference materials, Lexan 9034 (SABIC Innovative Plastic, MA) and paraffin wax (Polygon Corporation, MA), were tested using a single 200-μm Rockwell C diamond indenter of serial number G-209. Both
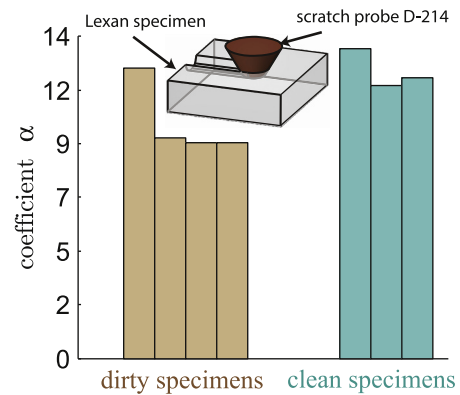
materials were selected for their homogeneous linear elastic isotropic mechanical behavior as well as their cost-effectiveness. Prior to testing, the fracture toughness of paraffin wax was characterized independently with single-edge notched bending tests, yielding a value of 0.082 MPa$\sqrt{m}$, which is an order of magnitude smaller than the fracture toughness of Lexan 9034, 2.69 MPa$\sqrt{m}$. Similarly, the uniaxial compressive strength of Lexan 9034, 86 MPa according to the manufacturer's specifications [33] is an order of magnitude greater than that of paraffin wax, 3.53 MPa [7]. Despite the significant difference in mechanical behavior, both Lexan 9034 and paraffin wax could be tested in the conical range, $d \geq 120$ μm by adjusting the maximum vertical force to 30 N for Lexan 9034 and 2 N for paraffin wax. Twenty-three scratch tests were carried out on a 25-mm square and 12-mm thick Lexan 9034 specimen prepared as detailed in Section 4.1 whereas eight scratch tests were carried out on a 50-mm $\times$ 25-mm $\times$ 6-mm thick specimen of paraffin wax prepared by following the steps 1,2 and 3 of the procedure described in Section 4.1. In particular, as displayed in Fig. 9(a) Lexan 9034 yields a conical calibration of 16.76 whereas paraffin wax yields 14.53. Nevertheless, both coefficients are close to the theoretical estimate and close to each other with a small relative error, 13%.

Furthermore, as shown in Fig. 9(b), the same probe, of serial number G-209, was employed to test a 25-mm square 12-mm thick specimen of impact-resistant light-weight polycarbonate provided by McMaster Carr, NJ and the scratch test results were analyzed using both calibrated shape functions–Lexan 9034 and paraffin wax. Both calibrations yielded a similar behavior of the quantity $F_T / \sqrt{2pA}$ that is expected to converge towards the bulk fracture toughness for large values of the ratio d/R; where F_T is the horizontal force measured on polycarbonate, 2 pA is the shape function of the Rockwell probe, d is the penetration depth measured on polycarbonate and $R = 200$ μm is the Rockwell probe tip radius. In this case, the relative error on the measured fracture toughness due to the choice of reference material, 7%, is small. Therefore, the calibrated shape function is intrinsic to the probe geometry and does not depend on the choice of a homogeneous, linear elastic isotropic reference material. Nevertheless, we recommend using Lexan 9034, according to the preparation protocol detailed in Section 4.1 in order to calibrate the scratch probe shape function.

5. Conclusion

The goal of this investigation was to present a systematic way to assess the fracture toughness via scratch tests through an
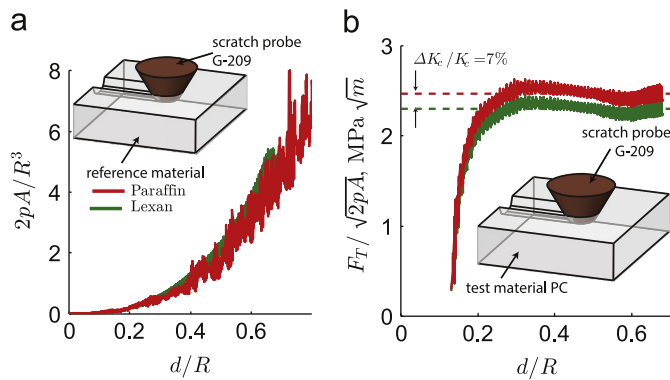
a

b

Fig. 9. (color online) Two calibration curves of the same 200-μm scratch probe, of serial number G-209, obtained by testing two different reference materials: a 50-mm × 25-mm × 12-mm specimen of paraffin wax and a 25-mm × 25-mm × 12-mm specimen of Lexan 9034. (b) Fracture characterization of a 25-mm × 25-mm × 12-mm specimen of polycarbonate (PC) via scratch tests performed with the 200-μm Rockwell C diamond probe, of serial number G-209, calibrated previously. Evolution of the quantity $F_T/\sqrt{2pA}$ as a function of the penetration depth d (in polycarbonate), using either the calibration function from paraffin wax or the one from Lexan 9034. In particular, the analytical model predicts that $F_T/\sqrt{2pA}$ will converge toward the fracture toughness of polycarbonate. 2 pA is the shape function of the scratch probe, G-209, $R = 200$ μm and F_T is the horizontal force measured while testing polycarbonate.

in-depth analysis of the failure mechanisms operating at both the macroscopic and microscopic length scales. First, we presented the Fracture Mechanics framework employed to derive the analytical expression of the fracture toughness as a function of the scratch forces, the probe geometry and the penetration depth, then, optical imaging and scanning electron microscopy were applied to paraffin wax, carbon steels and ceramic materials in order to verify the physical relevance of a fracture approach regarding scratch tests. At both the macroscopic and the microscopic scale, we witnessed a succession of multiple fracture events during single scratch test, each fracture event being characterized by a three-dimensional fracture surface with a crack front perpendicular to and a direction of crack propagation aligned with the scratch direction; these experimental observations perfectly agree with the assumptions of the theoretical model. Furthermore, advanced numerical simulations of crack growth in scratch tests, performed using the Finite Element software ABAQUS/CAE, revealed that the theoretical model is highly accurate even for large values of the back-rake angle and for large values of the friction coefficient and in the presence of a probe wear flat. On the other hand, at the microscopic scale, a meticulous specimen preparation procedure was designed to remove any imprecision in the fracture determination due to uncontrolled moisture content or surface contamination, thus making the method for fracture assessment via microscopic scratch tests repeatable, highly accurate and independent of the choice of reference material. Therefore this laborious theoretical, numerical and experimental endeavor has brought forward a novel application of scratch tests as a repeatable, robust and convenient means to characterize the fracture resistance at both the macroscopic and microscopic scales. Furthermore this research opens new venues for the multi-scale investigation of fracture processes in more complex and challenging materials such as cement paste, gas shale or cortical bone.

Acknowledgments

References

[1] ABAQUS 6.13, ABAQUS Analysis User's Guide, Dassault Systèmes, Providence, RI, USA, 2013.
[2] T.A. Adler, R.P. Walters, Wear and scratch hardness of 304 stainless steel investigated with a single scratch test, Wear 162–164 (1993) 713–720.
[3] A.-T. Akono, F.-J. Ulm, P. M. Reis, J. T. Germaine, Portable Scratch Testing Apparatus That Can Be Fixed on a Universal Testing Machine, Provisional Patent, Massachusetts Institute of Technology, 2013.
[4] A.-T. Akono, F.-J. Ulm, Fracture scaling for scratch tests of axisymmetric shape, J. Mech. Phys. Solids 60 (2012) 379–390.
[5] A.-T. Akono, N.X. Randall, F.-J. Ulm, Experimental determination of the fracture toughness via microscratch tests: application to polymers, ceramics, and metals, J. Mater. Res. 27 (2012) 485–493.
[6] A.-T. Akono, P.M. Reis, F.-J. Ulm, Scratching as a fracture process: from butter to steel, Phys. Rev. Lett. 106 (2011) 204302.
[7] A.-T. Akono, Scratch tests: a new way of evaluating the fracture toughness of materials (Master thesis), Massachusetts Institute of Technology, 2011.
[8] A.-T. Akono, F-J. Ulm, Scratch test model for the determination of fracture toughness, Eng. Fract. Mech. 78 (2010) 334–342.
[9] ASTM Standard C1624, Standard Test Method for Adhesion Strength and Mechanical Failure Modes of Ceramic Coatings by Quantitative Single Point Scratch Testing, ASTM International, West Conshohocken, PA, http://dx.doi.org/10.1520/C1624-05R10, www.astm.org, 2005.
[10] N. Axen, L. Kahlman, I.M. Hutchings, Correlation between tangential force and damage mechanisms in the scratch testing of ceramics, Tribol. Int. 30 (1997) 467–474.
[11] G.I. Barenblatt, Scaling, Self-similarity, and Intermediate Asymptotics, Cambridge University Press, Cambridge, UK, 1996.
[12] R.S. Barsoum, On the use of isoparametric finite elements in linear fracture mechanics, Int. J. Numer. Methods Eng. 10 (1976) 25–37.
[13] M. Bonnet, A. Frangi, Analyse des Solides Déformables par la Méthode des Éléments Finis, Les Editions de l'École Polytechnique, Paris, 2007.
[14] B.J. Briscoe, P.D. Evans, E. Pelillo, S.K. Sinha, Scratching maps for polymers, Wear 200 (1996) 137–147.
[15] J.L. Bucaille, C. Gauthier, E. Felder, R. Schirrer, The influence of strain hardening of polymers on the piling-up phenomenon in scratch tests: experiments and numerical modelling, Wear 260 (2006) 803–814.
[16] S.J. Bull, E.G. Berasetegui, An overview of the potential of quantitative coating adhesion measurement by scratch testing, Tribol. Int. 39 (2006) 91–114.
[17] S.J. Bull, Failure mode maps in the thin film scratch adhesion test, Tribol. Int. 30 (1997) 491–498.
[18] R. Consiglio, N.X. Randall, B. Bellaton, J. von Stebut, The nano-scratch tester (NST) as a new tool for assessing the strength of ultrathin hard coatings and the mar resistance of polymer films, Thin Solid Films 332 (1998) 151–156.
[19] ⟨www.csm-instruments.com⟩.
[20] ⟨www.esplog.com⟩.
[21] S.T. Gonczy, N. Randall, An ASTM standard for quantitative scratch adhesion testing of thin, hard ceramic coatings, Int. J. Appl. Ceram. Technol. 2 (2005) 422–428.
[22] A.A. Griffith, The phenomena of rupture and flow in solids, Philos. Trans. R. Soc. A 221 (1921) 163–198.
[23] R.W. Hertzberg, M.D. Skibo, J.A. Manson, Fatigue crack propagation in polyacetal, J. Mater. Sci. 13 (1978) 1038–1044.
[24] W. Kanematsu, Subsurface damage in scratch testing of Silicon Nitride, Wear 256 (2004) 100–107.
[25] P. Kurkcu, L. Andena, A. Pavan, An experimental investigation of the scratch behaviour of polymers: 1. influence of rate-dependent bulk mechanical properties, Wear 290–291 (2012) 86–93.
[26] S. Lafaye, C. Gauthier, R. Schirrer, Analyzing friction and scratch tests without in situ observation, Wear 265 (2006) 664–673.
[27] B.R. Lawn, E.R. Fuller, Equilibrium penny-like cracks in indentation fracture, J. Mater. Sci. 10 (1975) 20116–20124.
[28] M. Miller, C. Bobko, M. Vandamme, F-J. Ulm, Surface roughness criteria for cement paste nanoindentation, Cem. Concr. Res. 38 (2008) 467–476.
[29] D.M. Parks, The virtual crack extension method for nonlinear material behavior, Comput. Methods Appl. Mech. Eng. 12 (1977) 353–364.
[30] H. Pelletier, A.-L. Durier, C. Gauthier, R. Schirrer, Viscoelastic and elastic-plastic behaviors of amorphous polymeric surfaces, Tribol. Int. 41 (2008) 975–984.
[31] C.A. Pryde, P.G. Kelleher, M.Y. Hellman, R.P. Wentz, The hydrolitic stability of some commercially available polycarbonates, Polym. Sci. Eng. 22 (2004) 370–375.
[32] J.R. Rice, A path independent integral and the approximate analysis of strain concentration by notches and cracks, J. Appl. Mech. 35 (1968) 379–386.
[33] ⟨http://www.sabic-ip.com⟩.
[34] J.A. Williams, Analytical models of scratch hardness, Tribol. Int. 29 (1996) 675–694.
[35] M. Wong, G.T. Lim, A. Moyse, J.N. Reddy, H.-J. Sue, A new test methodology for evaluating scratch resistance of polymers, Wear 256 (2004) 1214–1227.